

Cluster Mass Estimate and a Cusp of the Mass Density Distribution in Clusters of Galaxies

Nobuyoshi Makino^{1,2} and Katsuaki Asano¹

¹Department of Physics, Ritsumeikan University

Kusatsu, Shiga 525-8577, Japan

²Department of Mechanical Engineering, Oita National College of Technology, 1666 Maki, Oita 870-0152,
Japan

e-mail: makino@oita-ct.ac.jp, sph10001@se.ritsumei.ac.jp

Received _____; accepted _____

ABSTRACT

We study density cusps in the center of clusters of galaxies to reconcile X-ray mass estimates with gravitational lensing masses. For various mass density models with cusps we compute X-ray surface brightness distribution, and fit them to observations to measure the range of parameters in the density models. The Einstein radii estimated from these density models are compared with Einstein radii derived from the observed arcs for Abell 2163, Abell 2218, and RX J1347.5-1145. The X-ray masses and lensing masses corresponding to these Einstein radii are also compared. While steeper cusps give smaller ratios of lensing mass to X-ray mass, the X-ray surface brightnesses estimated from flatter cusps are better fits to the observations. For Abell 2163 and Abell 2218, although the isothermal sphere with a finite core cannot produce giant arc images, a density model with a central cusp can produce a finite Einstein radius, which is smaller than the observed radii. We find that a total mass density profile which declines as $\sim r^{-1.4}$ produces the largest radius in models which are consistent with the X-ray surface brightness profile. As the result, the extremely large ratio of the lensing mass to the X-ray mass is improved from 2.2 to 1.4 for Abell 2163, and from 3 to 2.4 for Abell 2218. For RX J1347.5-1145, which is a cooling flow cluster, we cannot reduce the mass discrepancy.

Subject headings: dark matter — galaxies:clusters;general — gravitational lensing — X-rays: galaxies

1. Introduction

Masses of clusters of galaxies has been estimated based on observations of X-ray gas and by observation of gravitational lensing. Although cluster mass estimated by these methods should yield the same values, they generally are not, that is, the lensing mass is $2 \sim 3$ times larger than the X-ray mass (Grossman & Narayan 1989). The X-ray mass reflects the gas distribution weakly bound by the gravitational force. The predicted mass distribution has a large core radius. Conversely, the lensing mass distribution is strongly concentrated to produce distorted images around the center.

Many attempts have been made to reconcile the discrepancies between the X-ray and lensing mass measurements have been made. Mass models with ellipticity can reduce the mass required by the gravitational lensing (Miralda-Escudé 1993). However, the decrease is not so significant, especially, for Abell 1689 and Abell 2218 (Miralda-Escudé & Babul 1995). Miralda-Escudé & Babul (1995) presented a comparative analysis of lensing masses and X-ray masses, and found that a temperature two times higher than the observed value used be required to reconcile the discrepancy. Makino (1996) investigated the temperature distribution of the gas in lensing clusters, and showed that the gas temperature should significantly increase toward the center. The pressure of the diffuse magnetic field could support a gravitational force strong enough to produce giant arcs (Loeb & Mao 1994). However, this requirement for the magnetic field leads to higher Faraday rotation measures in the lensing cluster than in nearby clusters (Makino 1997). Moreover, Loeb & Mao (1994) proposed that in addition to the gas pressure, the bulk flow or turbulent motions in the cluster structure would contribute to the support of the X-ray gas. Gas dynamical simulations, however, cannot produce strong dynamical motions (Evrard, Metzler, & Navarro 1996).

Wu & Fang (1996) pointed out, by comparing the masses for samples of clusters derived from the X-ray to masses for samples from the gravitational lensing clusters, that the mass discrepancy is more significant around the cluster center than at large radii. Indeed, the discrepancy between the X-ray mass and the weak lensing mass is smaller than that between X-ray mass and the strong lensing mass which is derived from giant arc images. Moreover, the discrepancy in cooling flow clusters, which show strong peaks in the X-ray surface brightness at their centers, can be resolved by taking account of the effect of the peak in the surface brightness on the mass estimate (Allen, Fabian, & Kneib 1996; Allen 1997). This analysis is not applicable to the non-cooling flow clusters.

The cluster density distribution has so far been believed to be smooth and flat at the cluster center. Indeed, both isothermal spheres with finite core radii $\rho \propto 1/(r^2 + r_c^2)$ and modified King models, $\rho \propto 1/(r^2 + r_c^2)^{3/2}$ have been used to estimate the cluster mass. However, using N-body simulations of clusters of galaxies, Navarro, Frenk, & White (1997)

showed that density cusps form at the center, and that the density profiles have the same shape, independent of halo mass and of initial density fluctuation spectrum. According to them, the central density profile is well fit by an analytic form, $\rho \propto 1/[r(r + r_s)^2]$ (hereafter referred to as the NFW profile). The NFW profile is found in N-body/hydrodynamic simulations (Navarro, Frenk, & White 1995; Eke, Navarro, & Frenk 1997). Furthermore, Carlberg et al. (1997) found from measurements of galaxy velocity dispersions in clusters that the NFW profile can reproduce the measured velocity dispersion. At smaller scales, Hernquist (1990) derived an analytically approximated density profile, $\rho \propto 1/[r(r + r_s)^3]$ from the de Vaucouleurs law for the surface brightness of ellipticals. The Hernquist profile is in good agreement with numerical simulations (Dubinski & Carlberg 1991).

However, the value of the power of the density cusp at the center is controversial because of the affect of gravitational softening and poor resolution at small scales. Fukushige & Makino (1997) showed from simulations with particle numbers one order of magnitude higher, that typical central density profiles are shallower than $\rho \sim r^{-2}$ but steeper than $\rho \sim r^{-1}$. Moore et al. (1997) also derived steeper inner density profiles, $\rho \sim r^{-1.4}$ from cosmological N-body simulation with higher resolution. Furthermore, Evans & Collett (1997) found a steady-state, self-consistent, cusped solution of the collisional Boltzmann equation corresponding to $\rho \sim r^{-4/3}$. Their solution is not thermodynamically stable but is dynamically stable.

In this paper, we report on a study of the effect of density cusps in clusters of galaxies on the lensing mass and the X-ray mass. Assuming simple cluster mass models with cusps, i.e. spherically symmetric clusters with isothermal gas, we explicitly show that it is possible that the density cusp at the cluster center reduces the mass discrepancy between the X-ray mass and the lensing mass. In §2 we show our two step method: first we fix the parameters in the mass density models by comparing the estimated X-ray surface brightness profiles with the observed ones, and second, derive the estimated Einstein radii in the models and compare them with the observed Einstein radii from arcs. In §3, our method is applied to the observation of the lensing clusters, Abell 2163, Abell 2218 and RX J1347.5-1145, the X-ray masses and lensing masses are derived and the mass discrepancy are examined. In §4 we summarize our conclusions, and discuss our results.

Throughout this paper, we assume $H_0 = 50\text{km s}^{-1}\text{Mpc}^{-1}$, $\Omega_0 = 1$ and $\Lambda_0 = 0$.

2. Method of analysis

We consider a spherically symmetric cluster of galaxies with an X-ray emitting gas cloud, which is massive and distant enough to produce giant arcs around the center. We assume that the gas cloud of temperature T is isothermal and in hydrostatic equilibrium, and that the

total mass density profile $\rho(r)$ in the cluster can be described by a cusped density profile,

$$\rho(r) = \frac{\rho_0}{x^\mu(1+x^\nu)^\lambda}, \quad (1)$$

where ρ_0 is the normalization parameter and $x = r/r_s$; r_s is the scaling parameter. For example, the mass density with $(\mu, \nu, \lambda) = (0, 2, 1)$ is an isothermal sphere with a finite core radius and $(1, 1, 2)$ corresponds to the NFW profile. N-body simulations show that mass densities at the cluster scale decline as r^{-3} at large radii (Navarro, Frenk, & White 1995; Navarro, Frenk, & White 1996). We adopt the parameters that satisfy $\mu + \nu\lambda = 3$, except for an isothermal sphere.

The gas density distribution, ρ_g , satisfies the equation of hydrostatic equilibrium:

$$\frac{kT}{\mu_m m_p} \frac{d \ln \rho_g}{dr} = -\frac{GM(r)}{r^2}, \quad (2)$$

where μ_m and m_p denote the mean molecular weight (we adopt $\mu_m = 0.59$ below) and the proton mass, respectively. Here we have neglected the contributions of gas and galaxies to the total mass $M(r)$ within a radius r . The total mass $M(r)$ is estimated by integrating equation (1), and the gas density profile is uniquely determined from equation (2), if the gas temperature is given by observation. The gas density is expressed by two parameters, r_s and b , defined as

$$b = \frac{8\pi G \mu_m m_p \rho_0 r_s^2}{27kT}. \quad (3)$$

For the NFW profile ($\mu = 1, \nu = 1, \lambda = 2$) one finds that the gas density profile has the analytic form:

$$\rho_g(r) = \rho_{g0} \exp \left[-\frac{27}{2} b \left(1 - \frac{\ln(1+x)}{x} \right) \right], \quad (4)$$

where ρ_{g0} is the central gas density (Makino, Sasaki, & Suto 1997).

To compare directly our gas density models with observation, we compute the X-ray surface brightness given by

$$I(\theta) \propto \int_{D_1\theta}^{r_{\text{cut}}} \frac{\rho_g^2}{\sqrt{r^2 - (D_1\theta)^2}} r dr, \quad (5)$$

where D_1 is the angular diameter distance of the cluster from the observer. We have introduced a finite cut-off radius r_{cut} to avoid divergence in equation (5). Since a mass density profile which falls off as r^{-3} at large radii cannot bind the isothermal gas, the gas density is flat at large radii. The flat gas density at infinity leads to divergence in the surface brightness.

A simpler mass density profile has been extensively used to obtain the cluster mass from X-ray observations (e.g., Henry, Briel, & Nulsen 1993; Elbaz, Arnaud, & Böhringer 1995).

The observed X-ray emission is conventionally fitted with an isothermal β -model (see, Sarazin 1988)

$$I(\theta) = I_0 \left[1 + \left(\frac{\theta}{\theta_c} \right)^2 \right]^{-3\beta + \frac{1}{2}}, \quad (6)$$

where I_0 is the central surface brightness, θ_c is the angular core radius of the X-ray surface brightness, and β is the slope parameter. In the β -model, the gas density given by from equation (6) with $r_{\text{cut}} = \infty$ is:

$$\rho_g(r) = \rho_{g0} \left[1 + \left(\frac{r}{r_c} \right)^2 \right]^{-3\beta/2}, \quad (7)$$

where $r_c = \theta_c D_1$. Substituting equation (7) into equation (2), one obtains the total mass. Furthermore, differentiating equation (2) with respect to r , one finds the total mass density profile

$$\rho(r) = \frac{3\beta kT}{4\pi G \mu_m m_p r_c^2} \frac{3 + (r/r_c)^2}{[1 + (r/r_c)^2]^2}. \quad (8)$$

This density distribution is different from the cusped density distribution in equation (1). The mass density in equation (8) is non-singular at the center. The cluster with a mass density given by (8) would not have a large enough mass to produce giant arcs around the center.

On the other hand, we know that clusters do produce giant arcs. This imposes constraints on possible mass distributions, independent of X-ray mass estimates. In spherically gravitational lensing, if a lens is on the line of sight to a background source, the source will appear as arc images around a radius θ_E at which the flux of a lensed image is apparently divergent in the limit of the geometrical optics. We refer to the radius θ_E as the Einstein radius. In observations of gravitational lensing we assume that the Einstein radius, θ_E , is equal to the distance from the lens center to the giant arcs.

Now for a cusped density profile we determine the parameters b and θ_s in equation (1) and (3) on the basis of X-ray data on the surface brightness, and we estimate the cluster mass and the X-ray Einstein radius, $\theta_{E,X}$ as follows. The X-ray estimated Einstein radius is independent of the observed radius θ_E , and the difference between the two reflects the mass discrepancy. In the case of a spherically symmetric lens, the Einstein radius is completely described by the surface mass density $\Sigma(\theta)$ defined by

$$\Sigma(\theta) = 2 \int_{D_1\theta}^{\infty} \frac{\rho(r)}{\sqrt{r^2 - (D_1\theta)^2}} r dr. \quad (9)$$

and the critical surface mass density

$$\Sigma_{\text{cr}} = \frac{c^2}{4\pi G} \frac{D_s}{D_1 D_{1s}}, \quad (10)$$

where D_s and D_{ls} are the angular diameter distances from the observer to the source and from the lens to the source, respectively. We define the projected mass within θ by the parameters b and r_s determined from X-ray observation

$$m(\theta) = 2\pi \int_0^\theta \Sigma(\theta') \theta' d\theta'. \quad (11)$$

The X-ray estimated Einstein radius should satisfy

$$m(\theta_{E,X}) = \pi \theta_{E,X}^2 D_1^2 \Sigma_{cr}, \quad (12)$$

where we use $\rho(r)$ with the parameters determined from the X-ray observation.

We define the projected lensing mass within the measured Einstein radius using the observed quantities, Σ_{cr} , θ_E , and D_1 , as follows:

$$m_{lens}(\theta_E) \equiv \pi \theta_E^2 D_1^2 \Sigma_{cr}. \quad (13)$$

Note that the definition of the projected lensing mass is applicable to the region θ_E because the giant arcs reflect the mass distribution within the measured Einstein radius only. Thus, the projected X-ray mass compared to the projected lensing mass is only constrained by the region within the measured Einstein radius θ_E .

We can estimate an Einstein radius from the density models. We define the projected X-ray mass by the mass surface density Σ , determined from the X-ray observation:

$$m_X(\theta_E) = 2\pi \int_0^{\theta_E} \Sigma(\theta') \theta' d\theta', \quad (14)$$

where we again use $\rho(r)$ with the above parameters determined by the X-ray observations. This $m_X(\theta_E)$ is the X-ray mass to be compared with the lensing mass.

For the NFW profile, we can analytically derive $m(\theta_E)$ from the mass distribution. The detailed derivation of the Einstein radius for the NFW profile was found in Bartelmann (1996) and Maoz et al. (1997). However, for most of our density models, the projected mass cannot be analytically estimated from the mass distribution. We numerically integrate the right hand of equation (11) to estimate the Einstein radius $\theta_{E,X}$.

Our method is summarized as follows: we compute the X-ray surface brightness for the various density mass models described by equations (1) and (8). The estimated surface brightness is fitted to the X-ray observation of lensing clusters to fix the parameters in the density models. Once the parameters are determined, we can compare the measured Einstein radius with the Einstein radius estimated from X-ray observation. We also estimate the projected mass and the Einstein radius for each density model.

3. Results

To study the effect of central mass concentration on the X-ray surface brightness and gravitational lensing, we adopt the following parameters in equation (1): $\nu = 1$ group; $(\mu, \nu, \lambda) = (1, 1, 2), (1.2, 1, 1.8), (1.4, 1, 1.6), (1.6, 1, 1.4), (1.8, 1, 1.2)$, and $\lambda = 1$ group; $(1, 2, 1), (1.2, 1.8, 1), (1.4, 1.6, 1), (1.6, 1.4, 1), (1.8, 1.2, 1)$. In addition to the cusped mass density, we compute the projected mass and the Einstein radius from the mass density derived from the β -model in equation (8), and from the isothermal sphere with a finite core radius for comparison. The cut-off radius is fixed as $r_{\text{cut}} = 10r_s$ in our calculation of equation (5). For the isothermal model $(\mu, \nu, \lambda) = (0, 2, 1)$, we exceptionally fix r_{cut} as $10^4 r_s$. The gas densities derived from the cusped density profiles are flat at radii $\geq 10r_s$. Since the cusped density profiles decline as r^{-3} , the gas density cannot be strongly bound. Unless the gas distribution at large radii declines faster than $r^{-0.6}$ corresponding to $\beta = 0.4$ in the β -model, the gas density at the radius $r \sim D_l \theta$ mainly contributes to the integral in equation (5). As will be shown below, the cut-off radius of $10r_s$ is larger than the radius in which X-ray emissions from the clusters are detected. Thus, the choice, $r_{\text{cut}} = 10r_s$, is reasonable for our aim. The general behavior of the surface brightness estimated from the cusped density profile for the $\nu = 1$ group is discussed in Suto, Sasaki, & Makino (1998).

We apply our method of estimations to three clusters, Abell 2163, Abell 2218 and RX J1347.5-1145. They are X-ray clusters in which giant arcs have been found. Their cluster redshifts, gas temperature and observed Einstein radii are summarized in Table 1. We also list the parameters of the β -model, β and θ_c , derived from our fitting results of the observed surface brightness in Table 1.

3.1. The X-ray surface brightness

We illustrate the behavior of the surface brightness derived from cusped density profiles. In Figure 1 we show the X-ray surface brightness estimated from the cusped profiles for $b = 0.7$. The surface brightness for density models with $\nu = 1$ is plotted in Figure 1(a). The solid line indicates the surface brightness for $(\mu, \nu, \lambda) = (1, 1, 2)$. The dotted line, short dotted line, long dotted line and dashed dotted line show the surface brightness profiles for $(\mu, \nu, \lambda) = (1.2, 1, 1.8), (1.4, 1, 1.6), (1.6, 1, 1.4)$, and $(1.8, 1, 1.2)$, respectively

The surface brightness profiles with the parameters $\mu = 1, 1.2$ and 1.4 are similar in shape. They show a flat core around the center and a steep power law shape at large radii. Makino et al. (1998) showed that the gas density for $\mu = 1$ is in good agreement with the β -model in equation (7) which gives a good fit to the surface brightness of real clusters of galaxies. Thus, the surface brightness profiles for $\mu = 1, 1.2$ and 1.4 are expected to agree

with the observation of clusters of galaxies. However, the surface brightness for $\mu = 1.8$ shows a single power law shape and no finite core. It would be difficult to fit the surface brightness for $\mu = 1.8$ to observations. For $\mu = 1.6$ the surface brightness is marginal. The core around the center deviates slightly from a flat profile. While its surface brightness could agree with cooling flow clusters, it is not a good fit to clusters with a flat and large core radius like the Coma cluster.

The decrease of the core radius for larger μ is due to the strong concentration of the mass density at the center for large μ . Especially for $\mu = 1.8$ the core radius is not found in Figure 1(a). The behavior of the surface brightness for $\mu = 1.8$ is substantially the same as $\mu = 2$. The gas density in the density model with $\mu = 2$ is divergent at the center. In order to see the behavior of gas density for $\mu = 2$, we expand the integrand in equation (2) around the center, $x \ll 1$:

$$-\frac{d \ln \rho_g}{d \ln r} \approx \frac{4\pi G \rho_0 \mu_m m_p}{kT} \frac{r_s^{3-\mu}}{r} \int_0^{r/r_s} x^{2-\mu} (1 - \lambda x^\nu) dx. \quad (15)$$

If $\mu = 2$, the right hand in equation (15) is finite at the limit $r \rightarrow 0$. The gradient of the gas density is finite at the center. The density model with $\mu = 2$ cannot have a flat core in surface brightness under the assumption of the isothermal gas. For $\mu = 1.6$, the X-ray core radius is extremely small.

In Figure 1(b) we plot the surface brightness for the parameters $(\mu, \nu, \lambda) = (1.2, 1.8, 1)$, $(1.4, 1.6, 1)$, $(1.6, 1.4, 1)$, and $(1.8, 1.2, 1)$. The surface brightness in the $\lambda = 1$ model is steeper than in the $\nu = 1$ model at large radii for the same value of b . It is evident from equation (15) that a cusped density profile with a smaller ν and a larger λ has a larger core radius. For example, the surface brightness for $(\mu, \nu, \lambda) = (1, 1, 2)$ in Figure 1(a) is flatter than that for $(1, 2, 1)$ in Figure 1(b).

3.2. Abell 2163

Abell 2163 is a distant and elliptical cluster of galaxies. It is classified as an Abell richness class 2 cluster. The redshift is $z_1 = 0.201$. Abell 2163 has a very high temperature of 12.4 keV (Holzapfel et al. 1997) and X-ray luminosity in the 2-10 keV band of $L_X = 6.0 \times 10^{45}$ ergs s⁻¹ (Elbaz et al. 1995). Two arcs have been observed around the central galaxy. The measured Einstein radius is 15''6, and its redshift is 0.728 (Miralda-Escudé & Babul 1995).

We fit the surface brightness of the cusped density profiles to the observations by the χ^2 minimization, and determined the values of b and θ_s . In Figure 2, we plot the observed X-ray surface brightness profiles of Abell 2163 derived from the *ROSAT* HRI images and the best-fit profiles for various (μ, ν, λ) and the β -model.

The center of the surface brightness profile is located on the X-ray maximum of the cluster emission. The errors are 1- σ errors and account for Poisson statistics. A flat exposure map is

assumed. That is, vignetting effects are not taken into account in the data. The original data analysis can be found in Elbaz et al. (1995).

All the models are good fits at large radii, but the behavior of the profile for each of our models is very different in the flat core region. The contribution of the density cusp to the surface brightness profile is significant in the flat core region. Thus, we confine our attention to the behavior of the best-fit profiles within θ_c below.

The best-fit profiles for the $(\mu, \nu, \lambda) = (0, 2, 1)$, $(1, 1, 2)$ and $(1.2, 1, 1.8)$ models are very similar each other. They approximately reproduce the core structure of the X-ray emission. These three profiles deviate slightly upwards from the β -model within θ_c toward the center. The surface profile for $(\mu, \nu, \lambda) = (1.4, 1, 1.6)$ model is steeper than the models with $\mu \leq 1.2$, but is within the error bars. The X-ray profiles of more centrally concentrated models, $(\mu, \nu, \lambda) = (1.6, 1, 1.4)$ and $(1.8, 1, 1.2)$ are too steep in the central region to agree with the innermost data point within the error bars. The best-fit profiles of these models become steeper as μ increases. This tendency is also seen in Figure 2(c) for the $\lambda = 1$ group. The behaviors of the profiles for the $\lambda = 1$ group within θ_c are slightly flatter than ones for the $\nu = 1$ group for the same value of μ . The deviation from the best-fit β -model for the $\lambda = 1$ group is relatively small.

From the reduced χ^2 values in Table 2(a) and Figure 3(a), we find that the β -model is the best fitting model for the X-ray emission in Abell 2163, and that the cusped density profiles for $\mu = 1, 1.2$ and 1.4 marginally agree with the data. It is apparent from Figure 3(a) that the reduced χ^2 values for the cusped models change over the range $1.3 \sim 1.8$, except for $\mu = 1.6$ and $\mu = 1.8$. Although we present the reduced χ^2 only for the $\nu = 1$ model, the behavior of the reduced χ^2 for the $\lambda = 1$ group is similar. The relatively large values of the reduced χ^2 are caused by substructures in Abell 2163 which appear in the X-ray image (Elbaz et al. 1995). If we could get rid of the contribution of the substructures, the models for $\mu \leq 1.4$ would be in agreement with the data.

We estimate the X-ray predicted Einstein radii $\theta_{E,X}$ and the projected masses m_X within the measured Einstein radius θ_E for Abell 2163. The projected lensing mass of Abell 2163 is estimated to be $4.13 \times 10^{13} M_\odot$. The results are summarized in Table 2. For the $\nu = 1$ model the mass ratio and Einstein radius ratio are plotted in Figure 3 (b) and (c). For the $\nu=1$ group, the ratios of the projected lensing mass to the projected X-ray mass monotonically approach one as μ increases, but none is less than one. Although a larger μ decreases the mass ratio m_{lens}/m_X , the deviation of the estimated X-ray surface brightness around the center from the data is significantly large. This tendency is also found in the ratio $\theta_{E,X}/\theta_E$. The ratio increases as μ increases for the $\nu = 1$ group. Interestingly, a finite Einstein radius can form in the cusped density profiles although the giant arcs cannot be produced in the density models with a finite core. This implies that the mass concentration around the center is required to produce giant arcs. From the X-ray and the lensing analysis, our best mass

density model is $(\mu, \nu, \lambda)=(1.4, 1, 1.6)$ for Abell 2163. This density profile increases toward the center as $\rho \propto r^{-1.4}$. The estimated Einstein radius for the our best model amounts to 47% of the observed value. The projected mass for our best model is 57% larger than the mass estimated from the best-fit β -model.

For the $\lambda=1$ group, we obtain the same results as for the $\nu = 1$ group from Table 2(a). We, however, note that the change in b for $\nu=1$ groups is less sensitive to μ than in the $\lambda=1$ groups. The mass discrepancy is not improved for the $\lambda=1$ group as significantly as for the $\nu=1$ group.

3.3. Abell 2218

Abell 2218 is an Abell richness class 4 cluster at $z_1=0.175$. The radial velocity dispersion of cluster galaxies is very high, 1370km s^{-1} (Le Borgne, Pello, & Sanahuja 1992). About 30 arcs have been identified in this cluster. The configuration of these arcs strongly suggests that this cluster has two mass clumps (Kneib et al. 1995). While there is a secondary bright clump around galaxy #244 in a optical observation (Pelló et al. 1992), the X-ray image shows only one maximum close to the position of the cD galaxy. We consider one giant arc #359 with a radius of $20''.8$. The redshift of the source galaxy is 0.702 (Miralda-Escudé & Babul 1995). This arc is mainly caused by the central clump around the cD galaxy. Thus, we can neglect the second mass clump. The X-ray luminosity, L_X , is 0.7×10^{45} ergs s^{-1} (0.1-2.4 keV), and the gas temperature is measured to be 7.2keV (Mushotzky & Loewenstein 1997). Birkinshaw & Hughes (1994) reported $\theta_c = 60''$ and $\beta = 0.65$. On the other hand, Markevitch (1997) reported that the X-ray emission within a core radius of $60''$ is resolved into several components. Markevitch speculated that this may be caused by lensed X-ray emission, a merger shock or a gas trail of an infalling subgroup, or both lensing and a merger. Under these assumptions, he reanalyzed the X-ray profile and obtained $\theta_c = 26''$ and $\beta = 0.49$. We do not consider this possibility. We simply fit the surface brightness data with our models and we ignore the substructures in the cluster.

In Figure 4, we show the observed X-ray surface brightness profiles of Abell 2218 derived from the *ROSAT* HRI images and the best-fit profiles for various values of (μ, ν, λ) . The analysis of the data for Abell 2218 is the same as for Abell 2163. The detailed description of the data analysis is found in Squires et al. (1996)

We also plot the best-fit β -model with $\beta = 0.56$ and $\theta_c = 53''$. The data points are smoothly distributed in comparison with the data of Abell 2163. The behavior of the best-fit profiles of the $\nu = 1$ and $\lambda = 1$ groups for Abell 2218 is basically similar to those for Abell 2163. All the profiles are in excellent agreement with the data in the power law region at large radii. All of the surface brightnesses estimated from the cusped models are steeper than

that from the best-fit β -model at the flat core region. The best-fit profile becomes steeper as μ increases. All of the profiles of the $\nu = 1$ group deviate from the error bars. The surface brightness of the $\lambda = 1$ group pass inside the error bars only for $\mu \leq 1.2$.

We list results of the lensing analysis for Abell 2218 in Table 2(b). For the $\nu = 1$ model, the results are plotted in Figure 3. The projected lensing mass of Abell 2218 is $6.3 \times 10^{13} M_{\odot}$. The mass ratio and the ratio of the Einstein radius change for the parameters b and r_s in similar fashion as for Abell 2163. The change of b and θ_s for Abell 2218 shows the same behavior in Table 2(a) for both $\nu = 1$ and $\lambda = 1$ groups. The reduced χ^2 values are smaller than the values for Abell 2163 because of the smoothness of the X-ray emission. As seen in the mass estimate for Abell 2163, both the isothermal sphere and the best fit- β -model mass models cannot produce giant arcs for Abell 2218. The cusped density models, however, produce finite Einstein radii, however these are less than the estimated radius. For cusped density models, the ratio, m_{lens}/m_X and $\theta_{E,X}/\theta_E$ approach one as μ increases. For Abell 2218, our best model is $(\mu, \nu, \lambda)=(1.4, 1, 1.6)$. The estimated Einstein radius for our best model for Abell 2218 corresponds to 16% of the observed value. The projected mass m_X for our best model is 27% larger than the β -model mass. We cannot reduce the mass discrepancy of Abell 2218 as significantly as we did for Abell 2163. This is mainly due to the different gas temperature of the two clusters.

3.4. RX J1347.5-1145

A distant ($z_1 = 0.451$) cluster RX J1347.5-1145 has two dominant galaxies. It is the most X-ray luminous cluster: $L_X = 7.3 \times 10^{45}$ ergs s^{-1} (0.1-2.4 keV) and $T=9.3$ keV (Schindler et al. 1997). The X-ray profile of this cluster has a strong peak. Schindler et al. (1997) noted that this strong peak is probably evidence of cooling flows. However, they could not find significant evidence for cool gas in the spectra. Two bright arcs are located at about $35''$ from the cluster center and are positioned on opposite sides of the central galaxy (Schindler et al. 1995). The redshift of these arcs is 0.81 (Sahu et al. 1998).

In Figure 5, we present the observed surface profile of RX J1347.5-1145 derived from the *ROSAT* HRI images (Schindler et al. 1997) and the best-fit profiles estimated from various models. As a result of fitting by the β -model, we find an extremely small core radius r_c of 56kpc in comparison with that of nearby clusters, $r_c \approx 250$ kpc (Jones & Forman 1984). Indeed, the core radii of Abell 2163 and Abell 2218 yield about 200-300kpc in our fitting. The observed profile is steeper than the the best-fit β -model inside the core radius. This steep profile with a small core radius is presumably evidence of cooling flows, as Schindler et al. (1997) suggested. As shown in Figure 5, all of the best-fit profiles computed from the cusped density profiles is steeper than the best-fit β -model. The surface brightness for $\mu \leq 1.6$ of

both $\nu = 1$ and $\lambda=1$ group are in excellent agreement with the data, because of the steepness of the data points at the center of this cluster.

The projected lensing mass of RX J1347.5-1145 is $6.26 \times 10^{14} M_{\odot}$. The uncertainty of the mass is caused by the unknown redshift of the lensed source galaxy. Table 2(c) indicates that the reduced χ^2 values in RX J1347.5-1145 are approximately equal to one for both the $\mu = 1$ and $\nu = 1$ groups, except for the models with $\mu = 1.8$. Thus, models with $\mu \leq 1.6$ are acceptable. However, the mass discrepancy is not decreased for RX J1347.5-1145. The estimated Einstein radius and the projected X-ray mass are almost unchanged, even if μ increases. The projected mass m_X for $(\mu, \nu, \lambda)=(1.6, 1, 1.4)$ model is only 7% larger than the β -model. This may be due to the small core radius of this cluster. The X-ray core radius θ_c of this cluster is smaller than the Einstein radius θ_E , although the X-ray core radius is large than the Einstein radius for the previous two clusters. As shown in Figure 5, the surface brightness profiles are almost unchanged at $\theta > \theta_c$, even if the model is changed. Therefore, we conclude that the projected mass discrepancy of RX J1347.5-1145 was not decreased by our method based on available *ROSAT* data. The *ROSAT* HRI data may be dominated by X-rays from the cooling flow, not from the cluster as a whole, however. To improve our analysis for RX J1347.5-114, we need the X-ray data from the cluster as a whole, and we should take cooling flows into account.

4. Conclusions and Discussion

We studied the effect of the density cusp on the mass cluster estimates. We compared the Einstein radii estimated from the density profile with a cusp with the observed radius. We showed that the marginally steep cusp, $\mu = 1.4$, reduces the discrepancy of the mass estimates for Abell 2163 and Abell 2218. The ratio of the lensing mass to the X-ray mass is improved from 2.2 to 1.4 for Abell 2163, and from 3 to 2.4 for Abell 2218.

We found that the clusters should have a density cusp at the center to reduce the discrepancy between the X-ray mass and the lensing mass. The cusped density model is consistent with the density profile found in the N-body simulations (Navarro et al. 1997). Navarro et al. (1997) concluded that the density profile behaves as $\sim r^{-1}$ toward the center. However, the more strongly cusped density profile at the center is expected to reconcile the mass discrepancy. In fact, our best model falls off $\rho \propto r^{-1.4}$ around the center. The density profiles of clusters of galaxies might be more strongly peaked at the center as Fukushige & Makino (1997) and Moore et al. (1997) have shown with N-body simulations.

Although the introduction of a cusp in the density profile is not sufficient to resolve the mass discrepancy, the density cusp mainly contributes to the reduction of the discrepancy. In

addition to density cusps, we should take into account the gas temperature decline, the second mass clump and the gas dynamical motion. We expect that ellipticity in the mass distribution plays an important role in resolving the discrepancy. Indeed, Bartelmann (1996) has shown that mass estimation under the assumption of a spherically symmetric mass distribution are likely to overestimate the mass by $\sim 30\%-50\%$. If the density cusp model reduces the ratio of the lensing mass to the X-ray mass m_{lens}/m_X to $1.3 - 1.6$, the mass discrepancy would be resolved by the adoption of a more detailed cluster model, especially elliptical mass distributions for non-cooling flow clusters (Asano & Makino 1998). For RX J1347.5-1145, the difference between the lensing mass and the X-ray mass was not improved. This may be due to cooling flows (Schindler et al. 1997). For this cluster the cooling flows should be taken into account (Allen 1997).

Furthermore, independent of X-ray observations it has been recognized that the cusped models with $1 \leq \mu \leq 1.4$ are more plausible in gravitational lensing analysis. Bartelmann (1996) pointed out that the NFW profile predicts large values of the radial magnification for the cluster of galaxies MS 2137. This problem implies that the corresponding sources must be surprisingly thin in the radial direction. Evans & Wilkinson (1997) have shown that lenses which have more singular density cusps than the NFW profile assuage Bartelmann’s problem. The result of Evans & Wilkinson, which was derived from the analysis of gravitational lensing, agrees well with our result.

We adopted a density model which declines as $\sim r^{-3}$ at large radii. However, the density profile at large radii is uncertain. In N-body simulations it is difficult to determine whether mass clumps at large radii are assigned to the cluster. In fact, the profile of the Hernquist model for elliptical galaxies decreases as $\sim r^{-4}$ at large radii. Dubinski & Carlberg (1991) have shown by numerical simulations that the profile of clustering objects falls off as $\sim r^{-4}$ at large radii. Furthermore, Markevitch & Vikhlinin (1997) have applied the mass density model $\rho \propto x^{-1}(1+x)^{1-\alpha}$ to Abell 2256, and fit the data with the surface brightness estimated from mass models for $\alpha < 5$. However, mass densities which decline faster than r^{-3} are less effective for the formation of giant arcs than our model.

Miralda-Escudé & Babul (1995) have studied how cusped density models resolve the mass discrepancy. They have shown that a cusped mass density produces a peak in the isothermal gas density around the center, and that the cusped density model is inconsistent with *ROSAT* PSPC data of Abell 2218, Abell 2163 and Abell 1689. The *ROSAT* PSPC data show extremely small errors. On the other hand, we have used the *ROSAT* HRI data, which have relatively large errors. The two detectors are very different in the spatial resolution and their backgrounds. In addition, the fit is sensitive to the existence of substructures in the clusters, and the results depend on the data. If the surface brightness estimated from our models is fit to the *ROSAT* PSPC data, the mass discrepancy would not be significantly reduced.

Lastly, we comment on the scaling parameter r_s in the NFW profile. By numerical

simulations of dark halos, Navarro, Frenk, & White (1996) predicted that the scaling parameter r_s is approximately several hundred kpc at the cluster mass scale. On the other hand, r_s derived from our analysis are about 1Mpc for the Abell 2163 and 2218 clusters. Namely, the size of r_c predicted by Navarro, Frenk, & White is smaller than the observed values. This problem has been already pointed out by Makino et al. (1997). Both Bartelmann (1997) and Evans & Wilkinson (1997) adopted the scaling parameter which satisfies the estimation by the numerical simulations of Navarro, Frenk, & White. Their results for MS 2137 will be altered by taking into account the constraint by X-ray observations.

We are grateful to Makoto Hattori, Yasushi Suto and Kenji Tomita for their helpful advices, and Doris Neumann for providing the X-ray surface brightness data of Abell 2163 and Abell 2218. We thank Sabine Schindler for kindly providing the *ROSAT* HRI data of RX J1347.5-1145 in ASCII format. Lastly, we appreciate Maxim Markevitch for kindly providing the *ROSAT* HRI images for Abell 2218.

References

- Allen, S. W. 1998, MNRAS 296, 392
- Allen, S. W., Fabian, A. C., & Kneib, J. P. 1996, MNRAS 279, 615
- Asano, K., & Makino, N. 1998 in preparation.
- Bartelmann 1996, A&A 313, 697
- Birkinshaw, M., & Hughes, J. P. 1994, ApJ 420, 33
- Carlberg, R. G., Yee, H. K. C., Ellingson, E., Morris, S. L., Abraham, R., Gravel, P., Pritchet, C. J., Smecker-Hane, T., Hartwick, F. D. A., Hesser, J. E., Hutchings, J. B., & Oke, J. B. 1997, ApJ 485, L13
- Dubinski, J., & Carlberg, R. 1991, ApJ 378, 496
- Eke, V. R., Navarro, J. F., & Frenk, C. S. 1997, to appear in ApJ (astro-ph/9708070)
- Elbaz, D., Arnaud, M., Böhringer, H. 1995 A&A 293, 337
- Evans, N. W., & Collett, J. L. 1997, ApJ 480, L103
- Evans, N. W., & Wilkinson, M. 1998, MNRAS 296, 800
- Evrard, A. E., Metzler, C. A., & Navarro, J. F. 1996, ApJ 469, 494
- Fukushige, T., & Makino, J. 1997, ApJ 477, L9
- Grossman, S. A., Narayan, R. 1989, ApJ 344, 637
- Henry, J. P., Briel, U. G. & Nulsen, P. E. J. 1993, A&A 271, 413
- Hernquist, L. 1990, ApJ 356, 359
- Holzzapfel, W. L., Arnaud, M., Ade, P. A. R., Church, S. E., Fischer, M. L., Mauskopf, P. D., Rephaeli, Y., Wilbanks, T. M., & Lange, A. E. 1997, ApJ 480, 449
- Jones, C., & Forman, W. 1984, ApJ 276, 38
- Kneib, J. P., Mellier, Y., Pelló, R., Miralda-Escudé, J., Le Borgne, J. -F., Böhringer, H., & Picat, J. -P. 1995, A&A 303, 27
- Le Borgne, J. F., Pello, R., & Sanahuja, B. 1992, A&AS 95, 87
- Loeb, A., & Mao, S. 1994, ApJ 435, L109
- Makino, N. 1996, PASJ 48, 573
- Makino, N. 1997, ApJ 490, 641
- Makino, N., Sasaki, S., & Suto, Y. 1998, ApJ 497, 555
- Maoz, D., Rix, H-W., Gal-Yum, A., Gould, A. 1997, ApJ 486, 75

- Markevitch, M. 1997, ApJ 483, L17
- Markevitch, M., & Vikhlinin, A. 1997, ApJ 491, 467
- Miralda-Escudé, J. 1993, ApJ 403, 497
- Miralda-Escudé, J., & Babul, A. 1995, ApJ 449, 18
- Moore, B., Governato, F., Quinn, T., Stadel, J., & Lake, G. 1998, ApJ, 499, L5
- Mushotzky, R. F., & Loewenstein, M. 1997, ApJ 481, L63
- Navarro, J. F., Frenk, C. S., & White, S. D. M. 1995, MNRAS 275, 720
- Navarro, J. F., Frenk, C. S., & White, S. D. M. 1996, ApJ 462, 563
- Navarro, J. F., Frenk, C. S., & White, S. D. M. 1997, ApJ 490, 493
- Pelló, R., Le Borgne, J. F., Sanahuja, B., Methez, G., Fort, B. 1992, A&A 266, 6
- Sarazin, C. 1988, X-ray Emissions from Clusters of Galaxies. Cambridge Univ. Press, Cambridge
- Sahu, K. C., Shaw, R. A., Kaiser, M. E., Baum, S. A., Ferguson, H. C., Hayes, J. J. E., Gull, T. R., Hill, R. J., Hutchings, J. B., Kimble, R. A., Plait, P., & Woodgate, B. E. 1998, ApJ 492, L125
- Schindler, S., Guzzo, L., Ebeling, H., Böhringer, H., Chincarini, G., Collins, C. A., De Grandi, S., Neumann, D. M., Briel, U. G., Shaver, P., & Vettolani, G. 1995, A&A 299, L9
- Schindler, S., Hattori, M., Neumann, D. M., & Böhringer, H. 1997, A&A 317, 646
- Squires, G., Kaiser, N., Babul, A., Fahlman, G., Woods, D., Neumann, D. M., & Böhringer, H. 1996, ApJ, 461, 572
- Suto, Y., Sasaki, S., & Makino, N. 1998 in preparation.
- Wu, X. -P., & Fang, L. -Z. 1996, ApJ 461, L5

Figure captions

Fig. 1.— The X-ray surface brightness profiles estimated from the mass density models. The parameter b is equal to 0.7. (a) the surface brightness profiles for the $\nu = 1$ group. The solid line indicates the surface brightness for the models with the parameters $(\mu, \nu, \lambda) = (1, 1, 2)$. The dotted line, the short dashed line, the long dashed line, and the dotted-dashed line show the surface brightness for the models $(\mu, \nu, \lambda) = (1.2, 1, 1.8)$, $(1.4, 1, 1.6)$, $(1.6, 1, 1.4)$, $(1.8, 1, 1.2)$, respectively. (b) the surface brightness profiles for $\lambda = 1$ group. The solid line indicates the surface brightness for the models with the parameters $(\mu, \nu, \lambda) = (1, 2, 1)$. The dotted line, the short dashed line, the long dashed line, and the dotted-dashed line show the surface brightness for the models $(\mu, \nu, \lambda) = (1.2, 1.8, 1)$, $(1.4, 1.6, 1)$, $(1.6, 1.4, 1)$, $(1.8, 1.2, 1)$, respectively.

Fig. 2.— The X-ray surface brightness profile of the X-ray emission from Abell 2163. The boxes are the data of the observed surface brightness. The *ROSAT* HRI data were kindly provided to us by Doris Neumann. The solid lines are the best-fit β -model with parameters, $\beta = 0.54$ and $\theta_c = 65''$. (a) We present the surface brightness for the isothermal sphere with a finite core radius model and the $\nu = 1$ group for $\mu \leq 1.2$. The dotted line indicates the surface brightness for the isothermal sphere $(\mu, \nu, \lambda) = (0, 2, 1)$. The short dashed line and the long dashed line show the surface brightness for the cusped models with parameters $(\mu, \nu, \lambda) = (1, 1, 2)$ and $(1.2, 1, 1.8)$, respectively. (b) The X-ray surface brightness for the $\nu = 1$ groups with $\mu \geq 1.2$. The dotted line, short dashed line and the long dashed line show the surface brightness for the cusped models with parameters $(\mu, \nu, \lambda) = (1.4, 1, 1.6)$, $(1.6, 1, 1.4)$, and $(1.8, 1, 1.2)$, respectively. (c) The X-ray surface brightness for the $\lambda = 1$ groups with $\mu \leq 1.4$. The dotted line, short dashed line and the long dashed line show the surface brightness for the cusped models with parameters $(\mu, \nu, \lambda) = (1, 2, 1)$, $(1.2, 1.8, 1)$, and $(1.4, 1.6, 1)$, respectively.

Fig. 3.— The reduced χ^2 values, the ratios of the X-ray estimated Einstein radius to the observed Einstein radius and the ratios of the lensing mass to the X-ray mass for Abell 2163

and Abell 2218. We present the results only for the $\nu = 1$ group. The behavior for the $\lambda = 1$ group is similar to the $\nu = 1$ group. The solid lines and dotted lines indicate the quantities of Abell 2163 and Abell 2218, respectively. (a) the reduced χ^2 values for various values of the parameter μ . (b) the ratios of the X-ray estimated Einstein radius to the observed Einstein radius. (c) the ratios of the lensing mass to the X-ray mass

Fig. 4.— The X-ray surface brightness for Abell 2218. The *ROSAT* HRI data were kindly provided to us by Doris Neumann. The parameters for the best-fit β -model are $\beta = 0.56$ and $\theta_c = 53''$. We show the parameters for the other models in Table 2(b). (a) The surface brightness for the isothermal sphere with a finite core radius model and the $\nu = 1$ group for $\mu \leq 1.4$. The dotted line indicates the surface brightness for the isothermal sphere. The short dashed line, the long dashed line and the short and dashed line indicate the surface brightness profiles for the cusped models with parameters $(\mu, \nu, \lambda) = (1, 1, 2)$, $(1.2, 1, 1.8)$, and $(1.4, 1, 1.6)$ respectively. (b) The X-ray surface brightness for the $\lambda = 1$ groups with $\mu \leq 1.6$. The dotted line, short dashed line, the long dashed line and the short and long dashed line show the surface brightness for the cusped models with parameters $(\mu, \nu, \lambda) = (1, 2, 1)$, $(1.2, 1.8, 1)$, $(1.4, 1, 6.1)$ and $(1.6, 1.4, 1)$, respectively.

Fig. 5.— The X-ray surface brightness for RX J1347.5-1145. The *ROSAT* HRI data were kindly provided to us by Sabine Schindler. The parameters for the best-fit β -model are $\beta = 0.56$ and $\theta_c = 8.2''$. In Table 2(c), we show the parameters for the other models. (a) The surface brightness for the isothermal sphere with a finite core radius model and the $\nu = 1$ group for $\mu \leq 1.4$. The dotted line indicates the surface brightness for the isothermal sphere. The short dashed line, the long dashed line and the short and dashed line indicate the surface brightness profiles for the cusped models with parameters $(\mu, \nu, \lambda) = (1, 1, 2)$, $(1.2, 1, 1.8)$, and $(1.4, 1, 1.6)$ respectively. (b) The X-ray surface brightness in RX J1347.5-1145 for the $\lambda = 1$ groups with $\mu \leq 1.6$. The dotted line, short dashed line, the long dashed line and the short and long dashed

line show the surface brightness for the cusped models with parameters $(\mu, \nu, \lambda) = (1, 2, 1)$, $(1.2, 1.8, 1)$, $(1.4, 1, 6.1)$ and $(1.6, 1.4, 1)$, respectively.

Cluster	z_l	z_s	T	θ_E	θ_c	β
			keV	arcsec	arcsec	
Abell 2163	0.201	0.728	12.4	15.6	65	0.54
Abell 2218	0.175	0.702	7.2	20.8	53	0.56
RX J1347.5-1145	0.451	0.81	9.3	35	8.2	0.56

Table 1. Cluster sample. The parameters of β and θ_c are derived from our analysis.

(μ, ν, λ)	b	θ_c/θ_s	$\theta_{E,X}/\theta_E$	m_{lens}/m_X	reduced χ^2
β -model mass	-	-	-	2.24	1.32
(0, 2, 1)	0.15	1.9	-	2.01	1.55
(1, 1, 2)	0.63	0.25	0.10	1.75	1.51
(1.2, 1, 1.8)	0.56	0.15	0.27	1.62	1.55
(1.4, 1, 1.6)	0.54	0.064	0.47	1.43	1.76
(1.6, 1, 1.4)	0.49	0.015	0.72	1.23	2.63
(1.8, 1, 1.2)	0.39	0.00043	0.96	1.04	5.02
(1, 2, 1)	0.31	0.37	0.033	1.95	1.37
(1.2, 1.8, 1)	0.32	0.25	0.18	1.75	1.44
(1.4, 1.6, 1)	0.35	0.12	0.42	1.50	1.69
(1.6, 1.4, 1)	0.36	0.032	0.70	1.24	2.58
(1.8, 1.2, 1)	0.34	0.00067	0.89	1.10	5.12

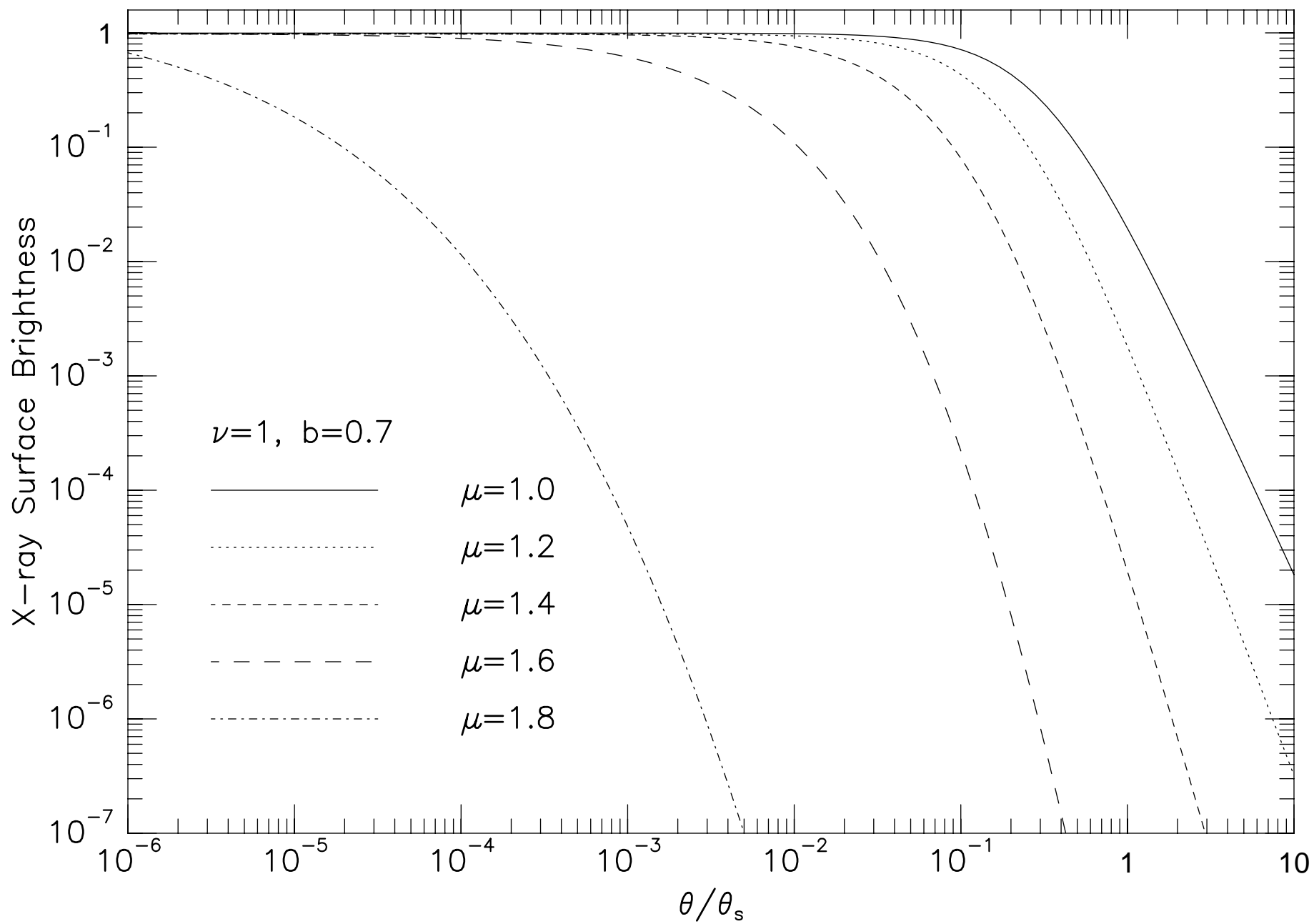
Table 2(a). Results for Abell 2163

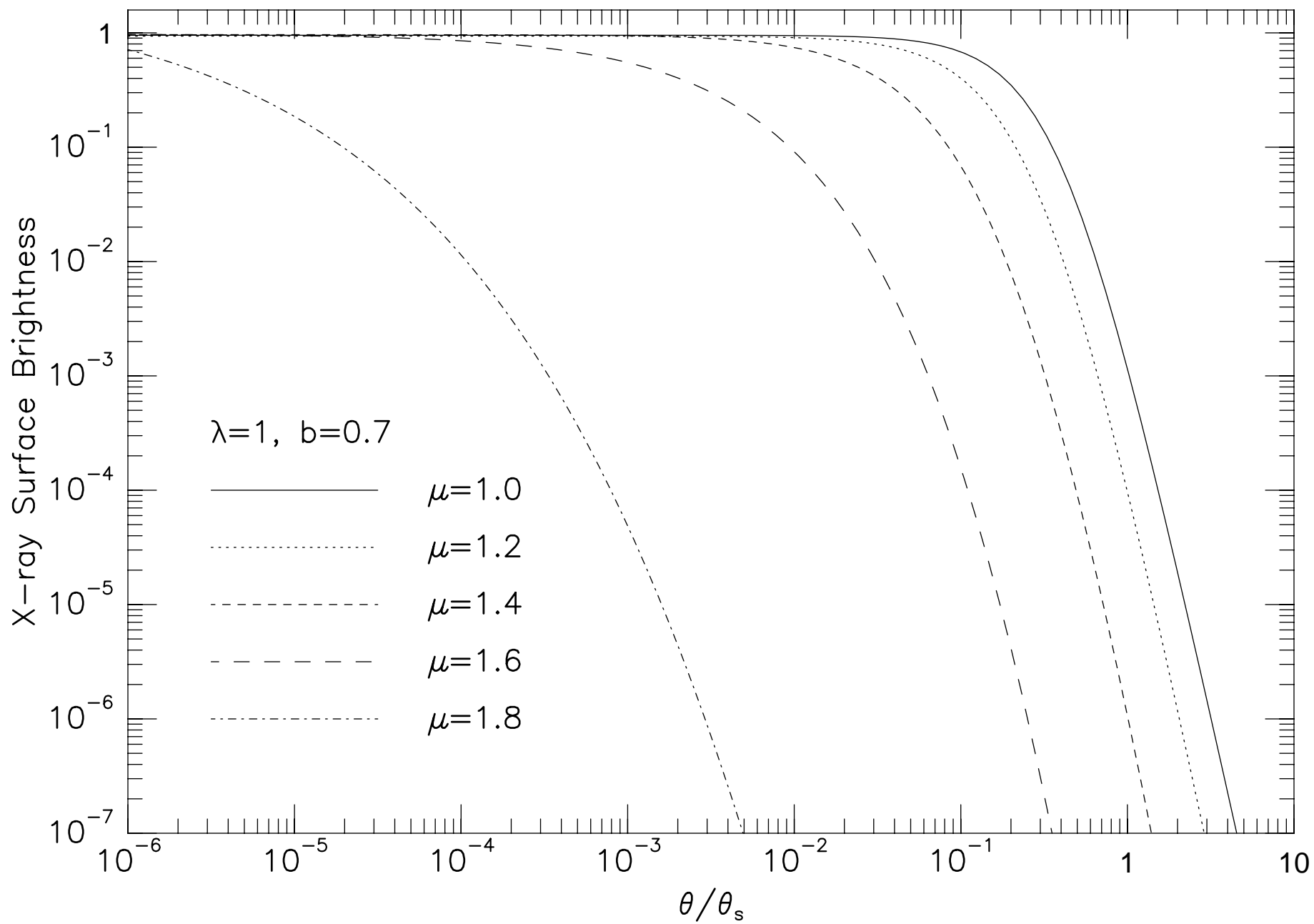
(μ, ν, λ)	b	θ_c/θ_s	$\theta_{E,X}/\theta_E$	m_{lens}/m_X	reduced χ^2
β -model mass	-	-	-	3.02	0.59
(0, 2, 1)	0.15	1.8	-	2.78	0.66
(1, 1, 2)	0.66	0.24	0.013	2.69	0.65
(1.2, 1, 1.8)	0.58	0.15	0.070	2.58	0.67
(1.4, 1, 1.6)	0.57	0.060	0.16	2.38	0.76
(1.6, 1, 1.4)	0.52	0.014	0.29	2.18	1.26
(1.8, 1, 1.2)	0.39	0.00047	0.42	2.00	2.76
(1, 2, 1)	0.33	0.37	0.0025	2.93	0.61
(1.2, 1.8, 1)	0.33	0.25	0.045	2.74	0.63
(1.4, 1.6, 1)	0.37	0.11	0.14	2.47	0.73
(1.6, 1.4, 1)	0.37	0.030	0.28	2.20	1.24
(1.8, 1.2, 1)	0.35	0.00063	0.39	2.11	2.82

Table 2(b). Results for Abell 2218

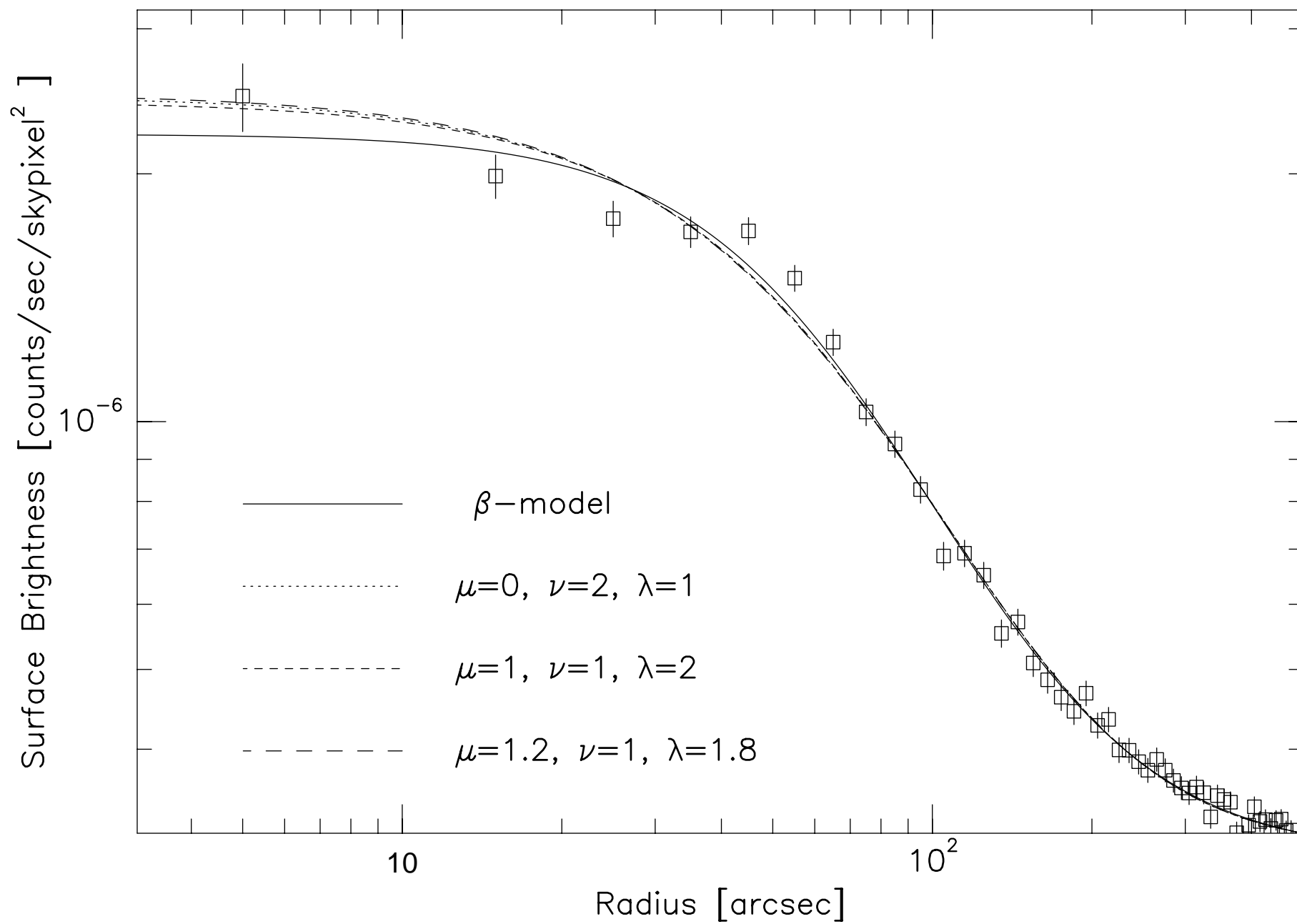
(μ, ν, λ)	b	θ_c/θ_s	$\theta_{E,X}/\theta_E$	m_{lens}/m_X	reduced χ^2
β -model mass	-	-	0.27	2.89	1.03
(0, 2, 1)	0.14	2.3	0.27	2.82	1.00
(1, 1, 2)	0.60	0.29	0.25	2.96	1.00
(1.2, 1, 1.8)	0.53	0.19	0.24	2.89	1.00
(1.4, 1, 1.6)	0.45	0.098	0.25	2.81	1.01
(1.6, 1, 1.4)	0.41	0.028	0.26	2.70	1.09
(1.8, 1, 1.2)	0.58	0.000089	0.25	3.00	1.66
(1, 2, 1)	0.32	0.39	0.23	3.12	1.02
(1.2, 1.8, 1)	0.31	0.27	0.24	2.98	1.01
(1.4, 1.6, 1)	0.31	0.16	0.24	2.87	1.01
(1.6, 1.4, 1)	0.30	0.056	0.25	2.77	1.08
(1.8, 1.2, 1)	0.47	0.00031	0.26	2.93	1.65

Table 2(c). Results for RX J1347.5-1145

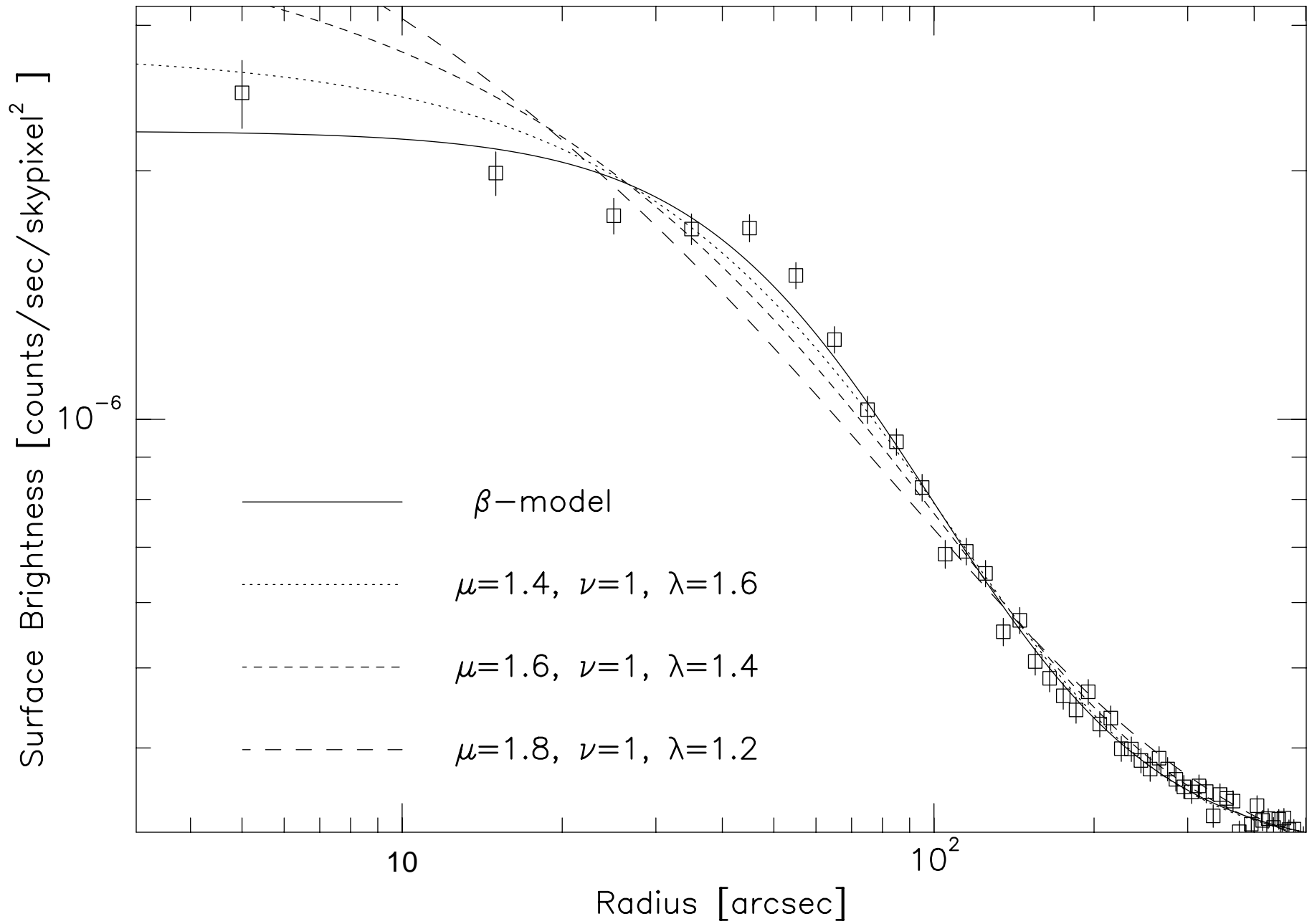




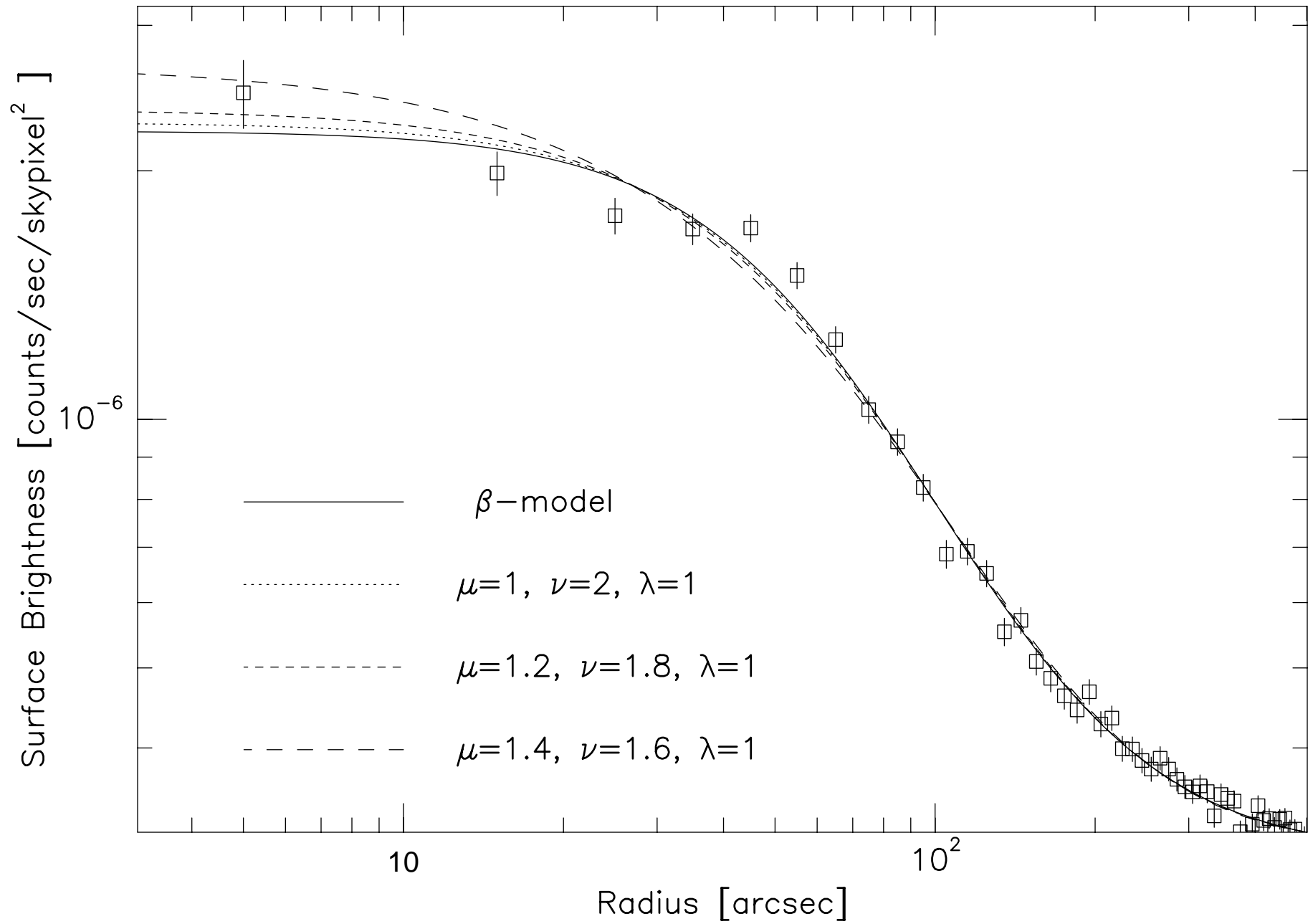
Abell 2163

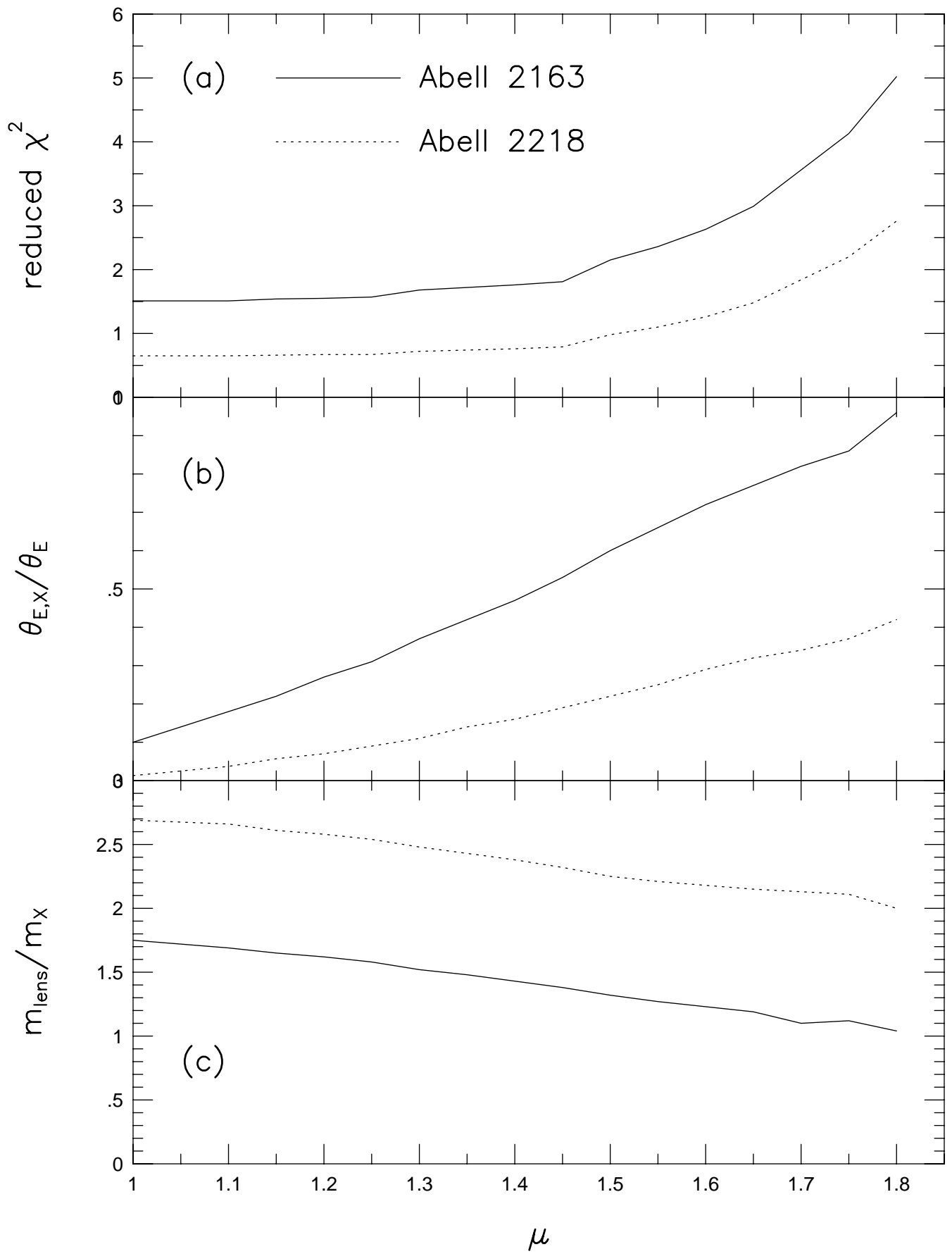


Abell 2163

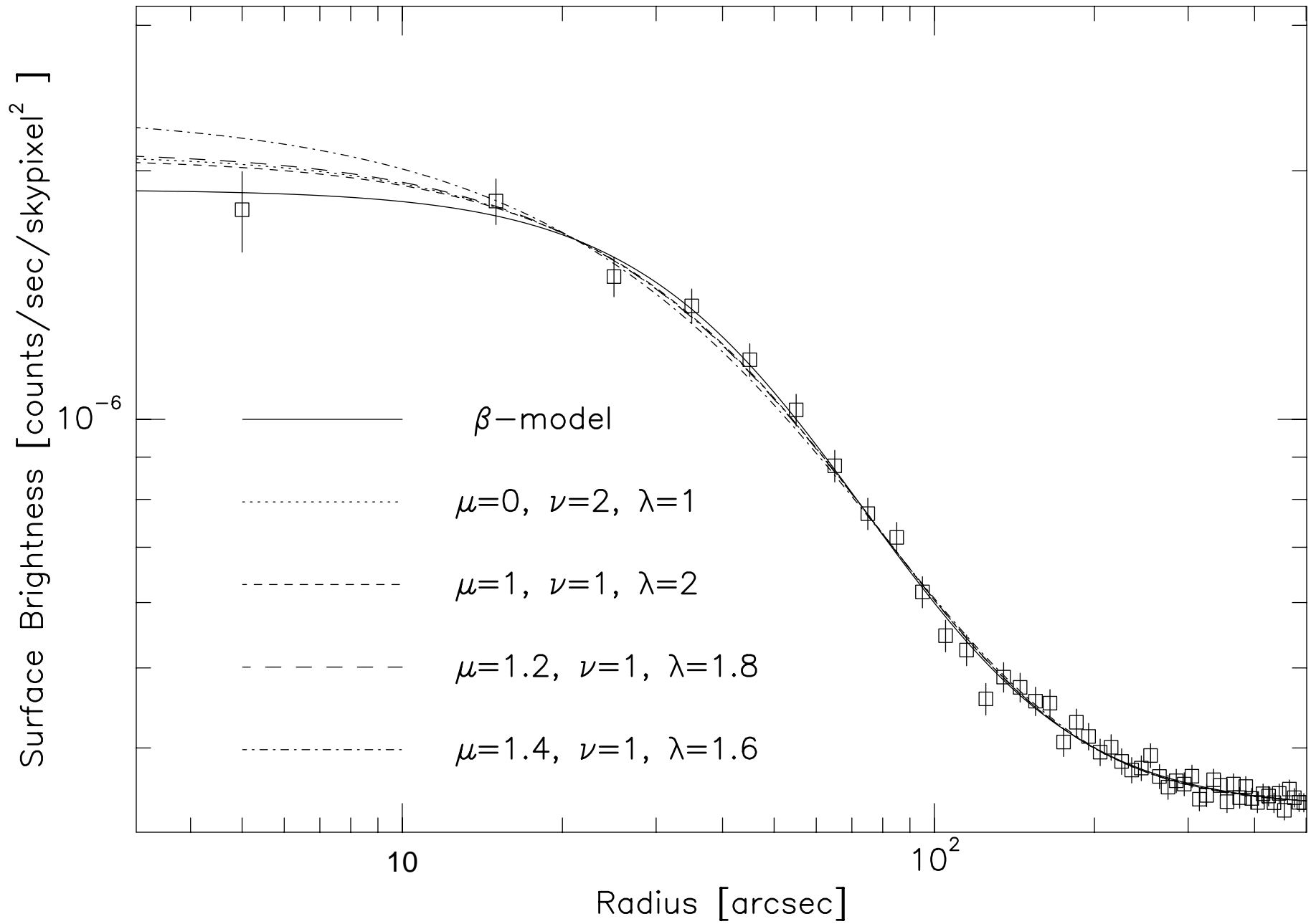


Abell 2163

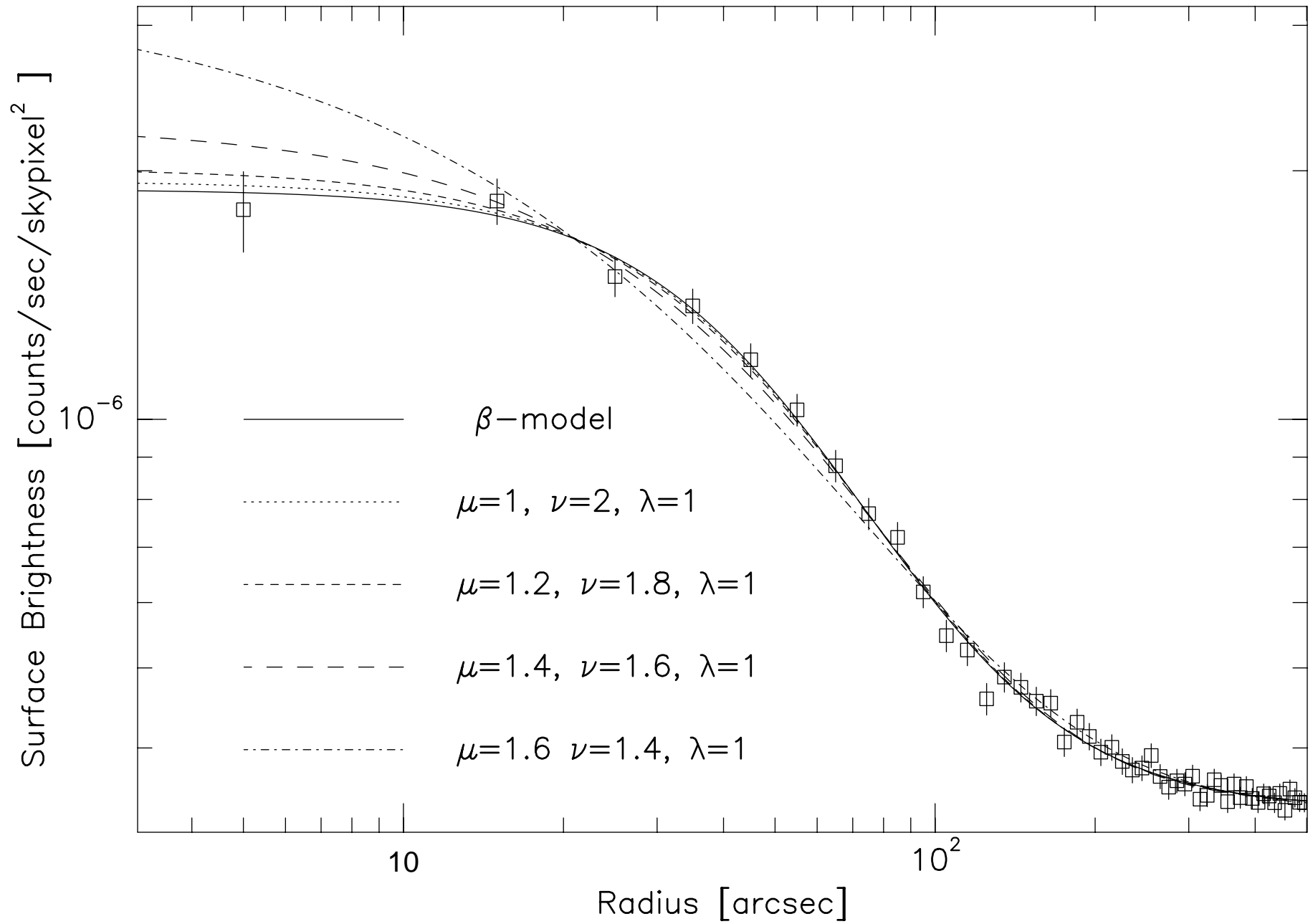




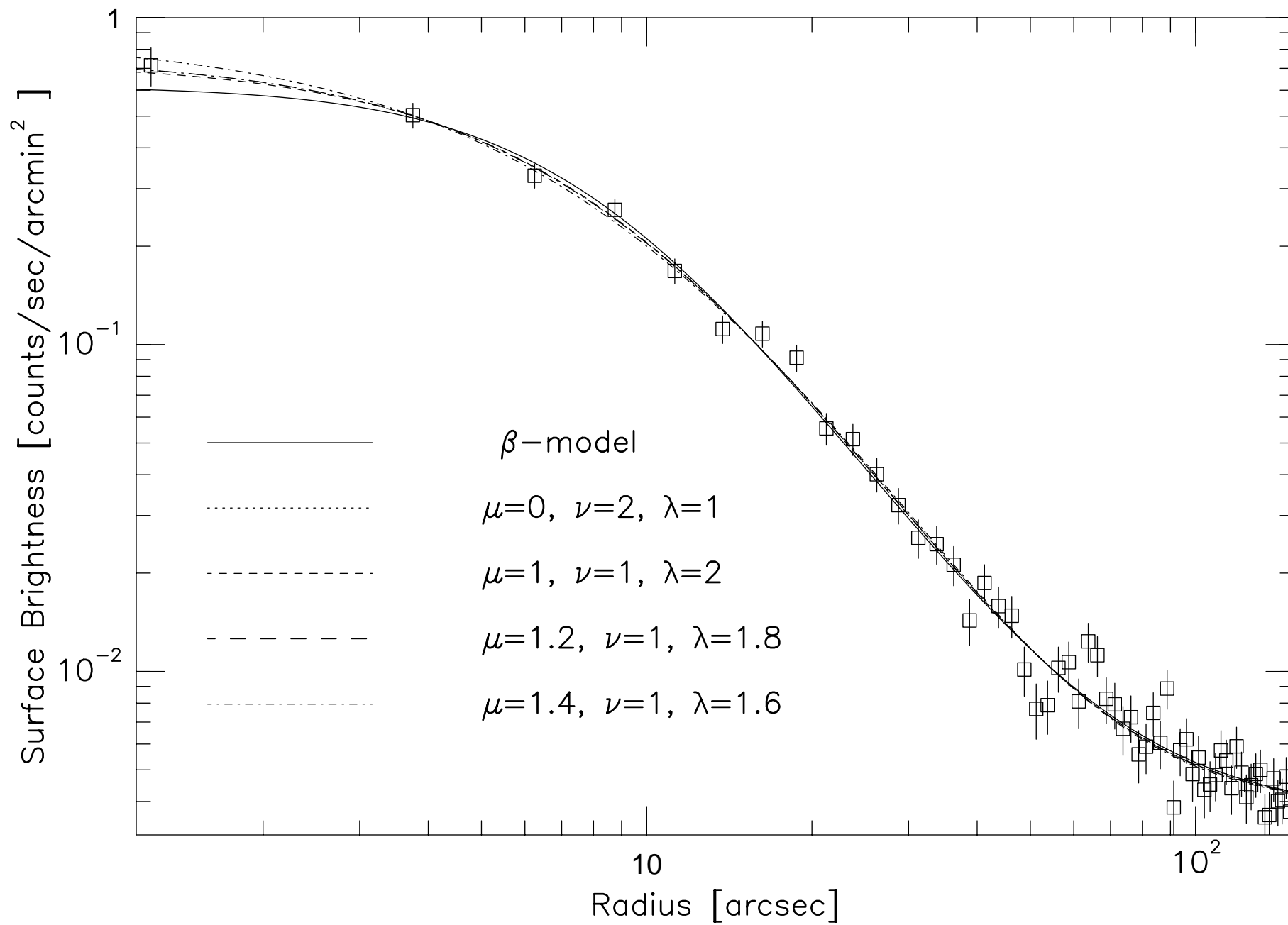
Abell 2218



Abell 2218



RX J1347.5-1145



RX J1347.5-1145

